

RESEARCH ARTICLE

10.1002/2013JA019207

Key Points:

- We report on the first direct observation of sputtered lunar oxygen
- We infer an O surface density of $1.3E7\text{ m}^{-3}$ and a column density of $1.6E13\text{ m}^{-2}$
- In addition, we provide the first measurements of backscattered solar wind He

Correspondence to:

A. Vorburger,
vorburger@space.unibe.ch

Citation:

Vorburger, A., P. Wurz, S. Barabash, M. Wieser, Y. Futaana, M. Holmström, A. Bhardwaj, and K. Asamura (2014), First direct observation of sputtered lunar oxygen, *J. Geophys. Res. Space Physics*, 119, 709–722, doi:10.1002/2013JA019207.

Received 8 JUL 2013

Accepted 12 JAN 2014

Accepted article online 17 JAN 2014

Published online 14 FEB 2014

First direct observation of sputtered lunar oxygen

A. Vorburger¹, P. Wurz¹, S. Barabash², M. Wieser², Y. Futaana², M. Holmström²,
A. Bhardwaj³, and K. Asamura⁴

¹Physikalisches Institut, University of Bern, Bern, Switzerland, ²Swedish Institute of Space Physics, Kiruna, Sweden, ³Space Physics Laboratory, Vikram Sarabhai Space Center, Trivandrum, India, ⁴Institute of Space and Astronautical Science, Sagami, Japan

Abstract We present the first direct measurement of neutral oxygen in the lunar exosphere, detected by the Chandrayaan-1 Energetic Neutral Analyzer (CENA). With the lunar surface consisting of about 60% of oxygen in number, the neutral oxygen detected in CENA's energy range (11 eV–3.3 keV) is attributed to have originated from the lunar surface, where it was released through solar wind ion sputtering. Fitting of CENA's mass spectra with calibration spectra from ground and in-flight data resulted in the detection of a robust oxygen signal, with a flux of 0.2 to 0.4 times the flux of backscattered hydrogen, depending on the solar wind helium content and particle velocity. For the two solar wind types observed, we derive subsolar surface oxygen atom densities of $N_o = (1.1 \pm 0.3) \cdot 10^7\text{ m}^{-3}$ and $(1.4 \pm 0.4) \cdot 10^7\text{ m}^{-3}$, respectively, which agree well with earlier model predictions and measured upper limits. From these surface densities, we derive column densities of $N_c = (1.5 \pm 0.5) \cdot 10^{13}\text{ m}^{-2}$ and $(1.6 \pm 0.5) \cdot 10^{13}\text{ m}^{-2}$. In addition, we identified for the first time a helium component. This helium is attributed to backscattering of solar wind helium (alpha particles) from the lunar surface as neutral energetic helium atoms, which has also been observed for the first time. This identification is supported by the characteristic energy of the measured helium atoms, which is roughly 4 times the energy of reflected solar wind hydrogen, and the correlation with solar wind helium content.

1. Introduction

The Moon has a very tenuous, surface-bound atmosphere, also called exosphere. The main sources that feed the lunar atmosphere are (1) thermal desorption, (2) backscattering of neutralized precipitating solar wind ions, (3) ion sputtering of lunar surface material by precipitating solar wind ions, (4) photon-stimulated desorption, and (5) micrometeoroid impact vaporization.

Thermal atmospheric desorption releases lunar volatile species such as Ar, Kr, CH₄, H₂, He, and Xe in the energy range 0.01–0.03 eV into the lunar exosphere [Wurz *et al.*, 2007]. The backscatter products are expected to resemble the main constituents making up the solar wind (H, He, and others [Wurz, 2001]) and have typical energies of up to 50% of the impinging solar wind energy [Futaana *et al.*, 2012]. Since sputtering releases lunar surface material located in the outermost layer of the lunar regolith, the main sputter products expected are O, Si, Mg, Ca, Al, Fe, and Na [Futaana *et al.*, 2006]. The characteristic energies of sputter products are 2–3 eV [Wurz *et al.*, 2007], but particles with energies of up to a few 100 eV are expected. Photon-stimulated desorption mainly releases lunar alkali species (Na, K), and possibly water, with characteristic energies between 0.1 eV and 0.4 eV from the lunar surface [e.g., Wurz and Lammer, 2003, and references therein]. Micrometeorite impact vaporization brings refractory elements in the energy range 0.2–0.4 eV into the exosphere [Wurz and Lammer, 2003; Wurz *et al.*, 2007]. Simulations show that micrometeorite impact vaporization and ion sputtering contribute approximately equally to the release of gas over the subsolar region for fluxes typical of the solar wind at 1 AU [Wurz *et al.*, 2007; Sarantos *et al.*, 2012].

Neutral species having so far been directly observed in the lunar atmosphere include He, Ar, Na, K, Rn, Po, H, and H₂. The first two species, He and Ar, were measured during the Apollo era by the Lunar Atmospheric Composition Experiment, which was deployed on the lunar surface by the Apollo 17 mission [Hoffman *et al.*, 1973; Hoffman and Hodges, 1975]. Rn and Po, both created in the lunar interior through radioactive decay, were detected by the Apollo 15 and 16 Alpha Particle Spectrometers [Gorenstein and Bjorkholm, 1973] and by the Alpha Particle Spectrometer onboard Lunar Prospector [Lawson *et al.*, 2005]. Potter and Morgan

[1988] and Tyler *et al.* [1988] reported on the ground-based spectroscopy detection of K and then Na in the lunar exosphere, with the Na to K ratio being the stoichiometric relative to the lunar surface. This suggests that these species are released from the lunar surface with a process that has similar yields such as impact vaporization and photon-stimulated desorption. Flynn and Stern [1996] searched for other constituents in the data of the spectrograph of the McDonald Observatory but could only determine upper limits for Si, Al, Ca, Fe, Ti, Ba, and Li and found that the species' densities relative to alkalis (Na and K) were more than an order of magnitude lower than a stoichiometric model would predict. Cook *et al.* [2013] and Stern *et al.* [2013] recently presented more stringent upper limits for many of these constituents and reported first H₂ measurements conducted by the Lyman Alpha Mapping Project instrument aboard NASA's Lunar Reconnaissance Orbiter.

McComas *et al.* [2009] and Wieser *et al.* [2009] presented first observations of backscattered neutral atoms from the lunar surface. Analyses of these measurements yielded unexpected high neutral hydrogen backscatter ratios of up to 0.25 [Vorburger *et al.*, 2013]. So far, only backscattered hydrogen neutrals and ions have been observed [e.g., McComas *et al.*, 2009; Wieser *et al.*, 2009; Saito *et al.*, 2008; Futaana *et al.*, 2010; Lue *et al.*, 2011].

To date, sputtered neutral lunar surface material has not been directly observed. Lunar surface sputtering, in contrast to laboratory sputtering, is a complex process, and the sputter yield is influenced by factors such as surface roughness, grain chemical heterogeneity, sputter site microslope, grain exposure dosage, and surface temperature [Stern, 1999]. Oxygen makes up more than 60% of the surface [Wurz *et al.*, 2007]; therefore, it is the most promising sputter product to look for.

2. Instrumentation

For this work we analyzed measurements conducted by the Sub-keV Atom Reflecting Analyzer (SARA) [Bhardwaj *et al.*, 2005; Barabash *et al.*, 2009] onboard the Chandrayaan-1 spacecraft [Goswami and Annadurai, 2009]. The mission operated from October 2008 until the end of August 2009, during which the spacecraft was first in a 100 km and later in a 200 km circular polar orbit. Chandrayaan-1's orbit around the Moon took about 2 h, half of which it spent on the sunlit side. SARA's main scientific goal was to investigate the interaction between the solar wind particles and the lunar surface. The instrument consisted of two sensors (i.e., two time-of-flight mass spectrometers) and a digital processing unit. Whereas the first sensor, the Solar Wind Monitor (SWIM) [McCann *et al.*, 2007], measured ions in the energy range 10 eV–15 keV, the second sensor, the Chandrayaan-1 Energetic Neutral Analyzer (CENA) [Kazama *et al.*, 2007] measured neutrals in the energy range 11 eV–2.2 keV. The two sensors were mounted at a 90° angle to each other, in such a way that CENA's 160° × 17° field of view was nadir looking (toward the lunar surface) and the 180° SWIM field of view pointed 90° to nadir. The fields of view of SWIM and CENA are divided into 15 and seven angular sectors [cf. Futaana *et al.*, 2010], respectively, which provide information about the particle's point of origin. In addition, both SWIM and CENA were capable of mass and energy discrimination. Since we used only CENA data for this analysis, we will only explain CENA's functional principle herein. Both sensors have very similar functional principles, though.

CENA consists of four subsystems [Bhardwaj *et al.*, 2005; Barabash *et al.*, 2009]: (1) an ion deflector responsible for rejecting charged particles from entering the instrument, (2) a conversion surface for positively ionizing the incoming neutral particles, (3) an energy analysis system blocking out photons and providing coarse energy analysis, and (4) a time-of-flight section responsible for mass analysis.

The electrostatic deflector at the entrance consists of two electrodes with a potential difference of 5 kV and sweeps out charged particles entering the system. The maximum rejection energy is 15 keV. Neutral particles, having passed the electrostatic deflector, strike a conversion surface made of a highly polished silicon wafer coated with MgO at grazing incidence. When interacting with the conversion surface, the neutral particles are converted with a certain efficiency to positive ions [Wieser *et al.*, 2002]. The positively ionized particles then have to pass a wave-type electrostatic analyzer. The electrostatic analyzer consists of electrodes of controlled potential. By varying the electrodes' potentials coarse energy analysis is achieved. In addition to the energy analysis, the electrostatic analyzer is able to effectively block out UV photons. Before particles reach the time-of-flight section, they are post accelerated by a voltage of about 1.5 keV to reduce

spreading in energy caused by the interaction with the conversion surface and to increase the mass resolution of the time-of-flight analysis. The post accelerated particles then enter the time-of-flight section where they hit a highly polished monocrystalline tungsten START surface and produce secondary electrons. These electrons are detected by a START microchannel plate assembly and produce a start pulse. The ions themselves, most of which have been neutralized upon interaction with the START surface, are reflected toward the STOP microchannel plates and produce a stop pulse. Since the distance traveled and the time required are known, the particles' velocities can be computed. These, together with the previous energy analysis, give the complete particles' mass and energy information.

Concerning measurement accuracy, three main sources introduce uncertainties in the particle's mass spectra: (1) different conversion efficiencies for different species, (2) energy straggling at the interaction with conversion and START surfaces, and (3) angular scattering on the START surface resulting in time-of-flight distance spreading.

3. Methods

Table 1 in Wurz [2001] presents the elemental composition of the solar wind plasma. As one can see from this table, the solar wind consists of $\approx 96\%$ of hydrogen, of $\approx 4\%$ of alpha particles, and to $\approx 1\%$ of heavy elements (mostly carbon, nitrogen, oxygen, neon, magnesium, silicon, and iron). Concerning backscattered solar wind particles, hydrogen and helium are therefore the most promising elements to look for. The molecular fractions of four different lunar reference suite soils are presented in Wurz *et al.* [2007, Table 2]. According to this table the lunar surface consists of about 60% oxygen in number, about 17% silicon, about 7% aluminum, and to a few percent of carbon, magnesium, iron, sodium, titanium, calcium, manganese, and chromium. CENA's detection efficiency for the different species relies on the species' ionization potential (cf. section 2). Even though the ionization potential for oxygen is higher than the ionization potential of the other elements, its much higher abundance in lunar regolith more than makes up for this drawback. In addition, CENA's mass resolution is proportional to mass, i.e., the peak width is proportional to the peak position. This means that the oxygen peak is narrower and therefore better defined than the silicon peak (the second most abundant element in the lunar surface) and therefore better distinguishable from the background. Oxygen is therefore the most promising sputtered candidate to search in CENA's mass spectra.

The most common species expected to be coming from the sunlit lunar surface in CENA's energy range are H, He, and O. In addition, since CENA's UV shielding is not perfect, CENA also measures a small UV background. CENA's mass spectra are thus expected to be mainly a mixture of H, He, O, and UV. To resolve the measured mass spectra, we therefore first determined the reference mass spectra for H, He, O, and UV.

The spectral shape of the UV background signal was computed from 21 orbits that showed clear UV contamination, which occurred when the Sun vector pointed toward the center of CENA's aperture. Since the obtained average spectral shape still contained small variations due to the limited statistics, it was smoothed with a bin width of three. The UV background signal thus obtained is shown in Figure 1 (red long dashed lines).

Since hydrogen from the lunar surface in CENA's energy range has its main origin in solar wind backscattering, we searched for orbits where the hydrogen content in the solar wind is more than 99.7%, i.e., orbits where the solar wind can be assumed to be purely hydrogen. Knowledge of the solar wind alpha to proton ratio (as well as of the particle velocity and the particle flux) was taken from the Solar Wind Experiment (WIND/SWE) data with a time resolution of 2 min (http://cdaweb.gsfc.nasa.gov/istp_public), which we time shifted from the L1 Lagrangian point to Chandrayaan-1's position in orbit around the Moon.

We found five such orbits, the average of which was again smoothed and which is shown in Figure 1 by the green dotted lines. Finally, the helium and oxygen reference mass spectra were computed from calibration data. They are shown by the blue dashed and purple dash-dotted lines in Figure 1, respectively. All reference mass spectra in Figure 1 are normalized to 1.

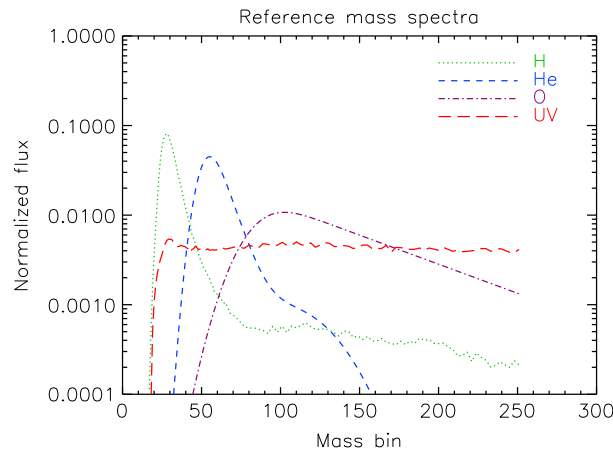


Figure 1. Hydrogen (green dotted), helium (blue dashed), oxygen (purple dash-dotted), and UV (red long dashed) reference mass spectra. All spectra are normalized to one.

In a second step, to resolve CENA’s mass spectra, the measured mass spectra were fitted with these four reference mass spectra using a nonnegative least squares solver. The fitting was carried out in two steps. First, the hydrogen and UV peaks, which dominate the mass spectra, were removed to obtain a signal which possibly contains backscattered helium and sputtered lunar oxygen, if these species are present in the mass spectra at all. The remaining residual was then fitted with the helium and oxygen reference mass spectra simultaneously. Equation (1) describes the two fitting steps:

$$MS_{CENA} = k_H \cdot MS_H + k_{UV} \cdot MS_{UV} + res_1$$

$$res_1 = k_{He} \cdot MS_{He} + k_O \cdot MS_O + res_2, \tag{1}$$

where MS_{CENA} is the mass spectrum measured by CENA, MS_H , MS_{He} , MS_O , and MS_{UV} are the reference mass spectra for hydrogen, helium, oxygen, and UV, respectively, k_H , k_{He} , k_O , and k_{UV} are the hydrogen, helium, oxygen, and UV fit coefficients determined by the nonnegative least squares solver, res_1 is the residual remaining after having fitted H and UV, and res_2 is the final remaining residual.

4. Results

To search for oxygen in CENA’s mass spectra we created two groups of CENA data: one group where the solar wind helium content was very low (<0.5%) and one group where the solar wind helium content was high (>3.5%). The two He contents were chosen so that each group contains at least 12 orbits. The reason for the creation of these two groups is that helium is a very effective sputter agent. According to *Wurz et al.* [2007], helium is 8 times as effective in sputtering as hydrogen, i.e., 5% of alpha particles typically contribute 30% of the total sputter yield. A significant difference in the ratio between the backscattered hydrogen and the sputtered oxygen flux is therefore expected for these two groups. For each group Tables 1 and 2 present the orbit numbers, the CENA time intervals for which we have corresponding WIND/SWE data (the complete CENA time interval is about 1 h), the WIND/SWE time intervals, and the average solar wind helium fraction, particle velocity, and particle flux. Note that the WIND time stamps denote the times when the measurements were taken and not the time-shifted time stamps mentioned above. Shown are the complete time intervals for which WIND/SWE data exists, but we only considered measurements where the quality flag was set equal to 10, i.e., “Solar wind parameters OK.” In addition, for both groups, the last row presents the average solar wind helium fraction, particle velocity, and particle flux.

For both groups, we computed the expected oxygen and hydrogen fluxes. Assuming that hydrogen in CENA’s energy range solely originates from backscattered solar wind protons and with oxygen being released from the lunar surface only through sputtering (cf. section 1), we compute the expected hydrogen flux according to backscatter theory and the expected oxygen flux according to sputter theory. For both species, the total flux at a certain energy given in [$s^{-1} cm^{-2} eV^{-1}$] is simply the product between the impinging solar wind flux, Φ_{sw} [$s^{-1} cm^{-2}$], either the oxygen sputter yield, Y_O^{sp} , or the hydrogen backscatter ratio, R_H , and the energy distribution function for sputtering or backscattering, $f_O^{sp}(E)$ [eV^{-1}] or $f_H^{bs}(E)$ [eV^{-1}], respectively,

$$\Phi_O^{sp}(E) = \Phi_{sw} \cdot Y_O^{sp} \cdot f_O^{sp}(E)$$

$$\Phi_H^{bs}(E) = \Phi_{sw} \cdot R_H \cdot f_H^{bs}(E). \tag{2}$$

Table 1. Orbits Making Up the Low Helium Content Group^a

Orbit Number	Start CENA (yyyy:ddd:hh:mm:ss)	Stop CENA (yyyy:ddd:hh:mm:ss)	Start SWE (yyyy:ddd:hh:mm:ss)	Stop SWE (yyyy:ddd:hh:mm:ss)	He Fraction (%)	V_{sw} (km/s)	Φ_{sw} ($10^{12} \text{ m}^{-2} \text{ s}^{-1}$)	Y_{O}^{SP} (10^{-2})
3026	2009 201 09 57 40	2009 201 12 05 24	2009 201 08 58 25	2009 201 11 08 51	0.20	308	4.19	6.1
3025	2009 201 07 49 51	2009 201 09 57 36	2009 201 06 51 11	2009 201 08 58 25	0.22	311	1.67	6.1
3033	2009 202 02 09 56	2009 202 02 33 08	2009 202 01 15 09	2009 202 01 37 60	0.26	323	6.96	6.1
2781	2009 179 16 18 27	2009 179 18 02 23	2009 179 15 10 36	2009 179 16 54 59	0.27	377	2.57	6.0
2947	2009 194 09 41 29	2009 194 10 53 13	2009 194 08 22 46	2009 194 09 32 54	0.28	345	1.57	6.0
3024	2009 201 07 34 51	2009 201 07 49 47	2009 201 06 36 30	2009 201 06 49 34	0.34	316	4.55	6.1
2656	2009 168 16 18 10	2009 168 16 36 42	2009 168 14 54 49	2009 168 15 11 08	0.36	300	6.96	6.1
3001	2009 199 04 42 50	2009 199 06 46 30	2009 199 03 35 34	2009 199 05 36 16	0.38	310	1.41	6.1
2599	2009 163 13 19 33	2009 163 15 27 01	2009 163 11 24 43	2009 163 13 38 18	0.41	293	2.13	6.2
3032	2009 201 23 20 40	2009 202 00 28 08	2009 201 22 22 19	2009 201 23 32 24	0.41	330	8.01	6.1
2447	2009 150 02 16 04	2009 150 03 56 24	2009 150 01 05 31	2009 150 02 43 18	0.44	369	1.72	6.0
3000	2009 199 02 40 51	2009 199 04 14 14	2009 199 01 34 54	2009 199 03 06 11	0.46	308	4.82	6.2
2999	2009 199 00 27 07	2009 199 02 20 18	2009 198 23 21 07	2009 199 01 12 02	0.46	311	2.86	6.2
2600	2009 163 15 27 05	2009 163 17 34 37	2009 163 13 38 18	2009 163 15 43 51	0.47	290	2.36	6.2
				average =	0.35	321	3.70	6.1

^a Shown are the orbit numbers, the CENA time intervals (year, day of year, hour, minute, second) for which we have corresponding WIND/SWE data, the WIND/SWE time intervals (year, day of year, hour, minute, second), the average solar wind helium fraction, particle velocity, particle flux, and the sputtering yield per solar wind ion. The last row presents the average solar wind helium fraction, particle velocity, particle flux, and oxygen sputter yield for the low helium content group.

Table 2. Orbits Making Up the High Helium Content Group^a

Orbit Number	Start CENA (yyyy:ddd:hh:mm:ss)	Stop CENA (yyyy:ddd:hh:mm:ss)	Start SWE (yyyy:ddd:hh:mm:ss)	Stop SWE (yyyy:ddd:hh:mm:ss)	He Fraction (%)	v_{sw} (km/s)	Φ_{sw} ($10^{12} \text{ m}^{-2} \text{ s}^{-1}$)	$\gamma_{\text{O}}^{\text{SP}}$ (10^{-2})
2945	2009 194 05 25 52	2009 194 07 33 36	2009 194 04 05 08	2009 194 06 12 20	3.65	338	2.23	7.2
2964	2009 195 21 54 06	2009 196 00 01 50	2009 195 21 04 20	2009 195 23 11 31	3.67	520	2.16	6.1
2963	2009 195 19 46 18	2009 195 21 54 02	2009 195 18 58 44	2009 195 21 04 20	4.22	531	2.28	6.1
2956	2009 195 04 51 42	2009 195 06 56 18	2009 195 04 01 47	2009 195 06 07 19	4.27	540	1.90	6.0
2930	2009 192 21 29 22	2009 192 23 37 06	2009 192 20 21 57	2009 192 22 27 29	4.33	427	2.26	6.9
2929	2009 192 19 21 34	2009 192 21 29 18	2009 192 18 14 44	2009 192 20 21 57	4.39	433	2.23	6.8
2944	2009 194 03 18 04	2009 194 05 25 48	2009 194 01 57 53	2009 194 04 05 08	4.53	342	2.24	7.5
2962	2009 195 17 38 30	2009 195 19 46 14	2009 195 16 48 15	2009 195 18 58 44	4.53	528	2.08	6.2
2955	2009 195 02 43 57	2009 195 04 51 38	2009 195 01 54 35	2009 195 04 01 47	4.74	542	2.09	6.1
2961	2009 195 16 07 02	2009 195 17 38 26	2009 195 15 18 33	2009 195 16 48 15	5.17	527	2.67	6.3
2928	2009 192 17 13 50	2009 192 19 21 30	2009 192 16 05 55	2009 192 18 14 44	5.49	433	2.26	7.1
2954	2009 195 00 36 09	2009 195 02 43 53	2009 194 23 39 15	2009 195 01 54 35	5.86	505	2.28	6.6
			average =		4.57	472	2.22	6.6

^aShown are the orbit numbers, the CENA time intervals (year, day of year, hour, minute, second) for which we have corresponding WIND/SWE data, the WIND/SWE time intervals (year, day of year, hour, minute, second), the average solar wind helium fraction, particle velocity, particle flux, and the sputtering yield per solar wind ion. The last row presents the average solar wind helium fraction, particle velocity, particle flux, and oxygen sputter yield for the high helium content group.

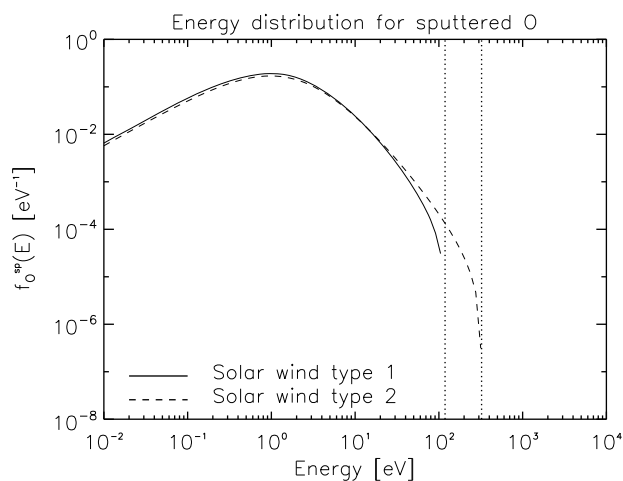


Figure 2. Energy distribution of sputtered lunar oxygen as given in Wurz *et al.* [2007, equation (1)], computed for an oxygen surface binding energy of 2 eV and two different solar wind types. Type 1 has a He content of 0.35% and a proton velocity 321 km s⁻¹ (solid line), and type 2 has a He content of 4.57% and a proton velocity of 472 km s⁻¹ (dashed line). The dotted vertical lines show where the oxygen sputter yield curves become 0 (119 eV and 323 eV).

Wurz *et al.* [2007] and Futaana *et al.* [2012] presented $f_o^{sp}(E)$ and $f_H^{bs}(E)$, respectively. For convenience, we restate these two functions here

$$f_o^{sp}(E) = \frac{6E}{3 - 8\sqrt{E_b/E_c}} \frac{E}{(E + E_b)^3} \left\{ 1 - \sqrt{\frac{E + E_b}{E_c}} \right\}$$

$$f_H^{bs}(E) = \frac{E}{(kT)^2} \exp\left(-\frac{E}{kT}\right), \quad (3)$$

where E_b is the surface binding energy of the sputtered particle, E_c is the cutoff energy, i.e., maximum energy that can be transferred in a binary collision, and where kT is the characteristic energy, which is given by $kT = V_{sw} \cdot 0.273 - 1.99$.

A model describing sputter release from the lunar surface was presented by Wurz *et al.* [2007]. From Figure 2 presented therein, values for Y_o^{sp} can be directly obtained. As mentioned above, they also present a mathematical description of $f_o^{sp}(E)$. For our analysis, we computed $f_o^{sp}(E)$ for two solar wind types, the helium content and particle velocity of which are given by last rows of Tables 1 and 2, respectively. The oxygen binding energy was taken to be equal to 2 eV (according to simulations conducted using the TRIM software package (<http://www.srim.org/>)). The two thus computed sputtering curves are shown in Figure 2. As one can see from this figure, Y_o^{sp} becomes 0 at 119 eV and 323 eV (dotted vertical lines), respectively. This limit is given by the maximum energy that can be transferred in a binary collision. Any sputtered oxygen atom detected by CENA at energies higher than these two energy thresholds can therefore be considered to be background.

Analysis of the mass spectra was divided into two energy ranges, below and above 119 eV and 323 eV, respectively. The hydrogen, helium, oxygen, and UV fit as well as the total fit (=hydrogen+helium+oxygen+UV) fits for the low, and the high-energy mass spectra of the two helium content groups are presented in Figure 3 and Table 3, with energy thresholds as mentioned above. Note that helium was only determined to be present in the high-energy range of the high helium group. Figure 3d is therefore the only panel showing a helium curve. To allow easier comparison between the four different measured mass spectra, we present the normalized measured mass spectra associated with the low- and the high-energy ranges of the low and the high helium content groups in one plot, namely, in Figure 4. Also shown, for comparison, are the normalized helium and oxygen reference mass spectra, which were, for better visibility, divided by 100.

As expected, the oxygen fit is in both cases significantly higher in the low-energy part than in the high-energy part, where we theoretically should measure no oxygen at all.

In a first analysis, we compute the ratio between the sputtered oxygen contained in CENA's complete energy range between the low and the high helium group. The fit coefficients for CENA's complete energy range

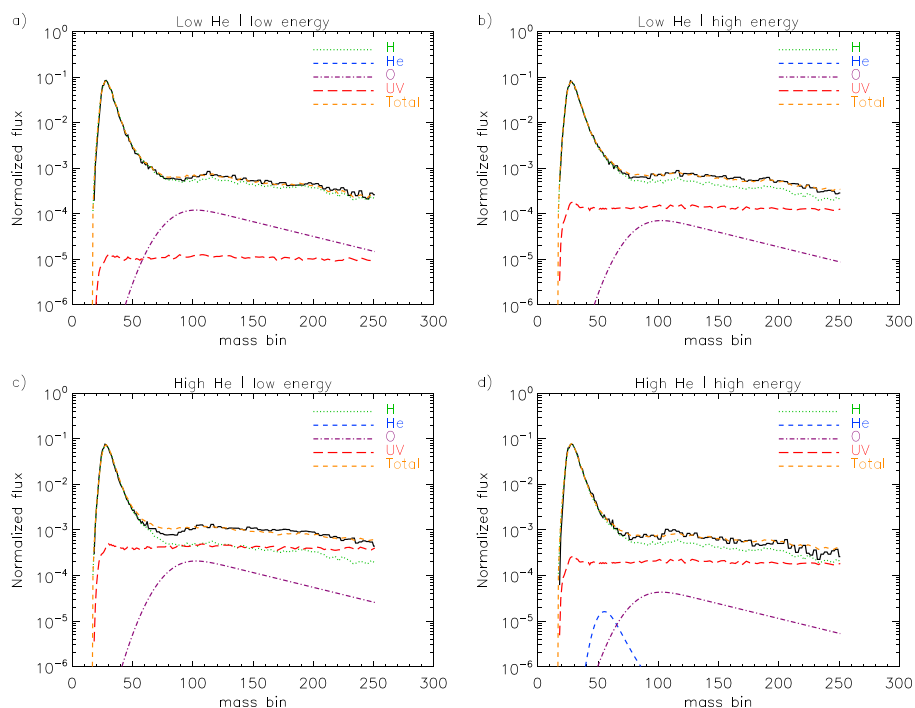


Figure 3. Average measured mass spectra (solid black) and the best fits for H (green dotted), He (blue dashed; where existent), O (purple dash-dotted) and UV (red long dashed). In addition, the sums of the fits (H + He + O + UV) are shown by the orange dashed line. (a and b) The low-energy part and the high-energy part of the low helium content group (<0.5% He), respectively, and (c and d) the low-energy part and the high-energy part of the high helium content group (>3.5% He), respectively. The division into low- and high-energy range occurs at 119 eV for the low helium group and at 323 eV for the high helium group.

are shown in the two bottom rows of Table 3, whereas the fits themselves are presented in Figure 5. Since we now compare the sputtered oxygen fluxes from two different solar wind types, the oxygen sputter yield, which is solar wind composition and velocity dependent, has to be taken into account. *Wurz et al.* [2007] present in Figure 2 sputter yields for solar wind consisting to 95% of H and to 5% of He. We recomputed these sputter yields for the actual solar wind helium fractions and present them also in Tables 1 and 2 (last column). The average sputter yields for the two solar wind types are ~ 0.06 and ~ 0.07 . In addition, we also take the surface porosity into account, since it linearly scales the sputter yield [cf. *Wurz et al.*, 2007, and references therein]. As *Wurz et al.* [2007] in their calculations, we use a porosity of 50%, which seems to be a good value for the porosity of the uppermost lunar surface layer. The average sputter yields are thus reduced to ~ 0.03 and ~ 0.035 . With these sputter yield values, the high helium content solar wind type was expected to sputter ≈ 1.2 times the oxygen from the lunar surface as the low helium content solar wind type. The ratio obtained from our fits is ≈ 1.6 .

In a second analysis, we compute the ratio between the backscattered hydrogen flux and the sputtered oxygen flux. The hydrogen backscatter ratio was recently computed from CENA data to be equal to 0.16 ± 0.05

Table 3. H, He, O, and UV Coefficients (cf. Equation (1)) Determined by the NonNegative Least Squares Solver for the Different Energy Ranges of the Low Helium (First Two Rows) and the High Helium Group (Rows Three and Four)^a

He Fraction	Energy Range	k_H	k_{He}	k_O	k_{UV}
low	low	1.002	0.000	1.111e-2	6.820e-8
low	high	0.968	0.000	0.655e-2	6.257e-7
high	low	0.899	0.000	1.933e-2	2.664e-6
high	high	0.958	3.577e-4	0.400e-2	9.116e-7
low	complete	0.984	0.000	0.851e-2	0.018
high	complete	0.918	0.000	1.369e-2	0.080

^aThe last two rows show the fit coefficients for CENA's complete energy range.

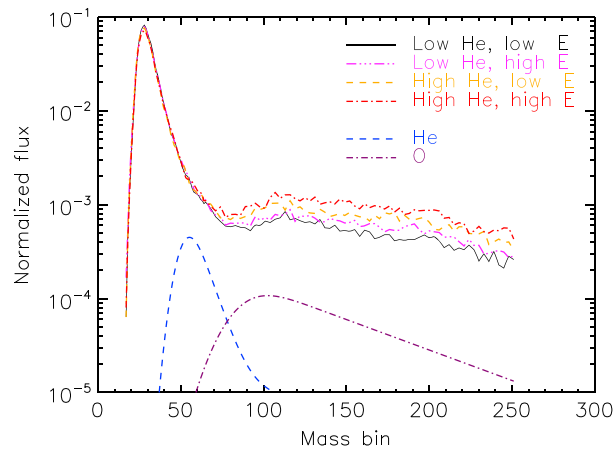


Figure 4. Comparison between the measured mass spectra presented in Figures 3a to 3d. Shown are the low-energy range of the low helium group (black solid), the high-energy range of the low helium group (magenta dash-dotted), the low-energy range of the high helium group (orange dashed), and the high-energy range of the high helium group (red dash-dotted). Also shown, for comparison, are the helium (blue dashed) and the oxygen (purple dash-dotted) reference mass spectra, which were, for better visibility, divided by 100.

at the subsolar point [Vorburger *et al.*, 2013], and the energy distribution curve for backscattered hydrogen (see above), also recently derived from CENA data, is given in Futaana *et al.* [2012]. To compare the theoretical fluxes to the fluxes measured by CENA we have to correct for CENA's different detection efficiencies for different species. In addition, we have to take into account that CENA only covers a certain fraction of the respective energy distributions. Figures 6a and 6b show the energy distribution functions for backscattered hydrogen and sputtered oxygen particles and the fluxes as they can theoretically be detected by CENA. Also shown, by the two dotted vertical lines, are CENA's lower and upper energy bounds (11 eV and 3.3 keV). As one can see from this figure, especially in the case of sputtering, only a fraction of the complete energy spectrum is observed by CENA. We thus derived the ratio $\hat{\epsilon}_O^{\text{det}}/\hat{\epsilon}_H^{\text{det}}$ (see Appendix A) that corrects for both the detection efficiency and CENA's energy interval. The ratio between the total backscattered hydrogen flux and the total sputtered oxygen flux can thus be computed from the measurements according to the following equation:

$$\left. \frac{\Phi_H^{\text{bs}}}{\Phi_O^{\text{sp}}} \right|_{\text{meas}} = \frac{k_H}{k_O} \cdot \frac{\hat{\epsilon}_O^{\text{det}}}{\hat{\epsilon}_H^{\text{det}}}, \quad (4)$$

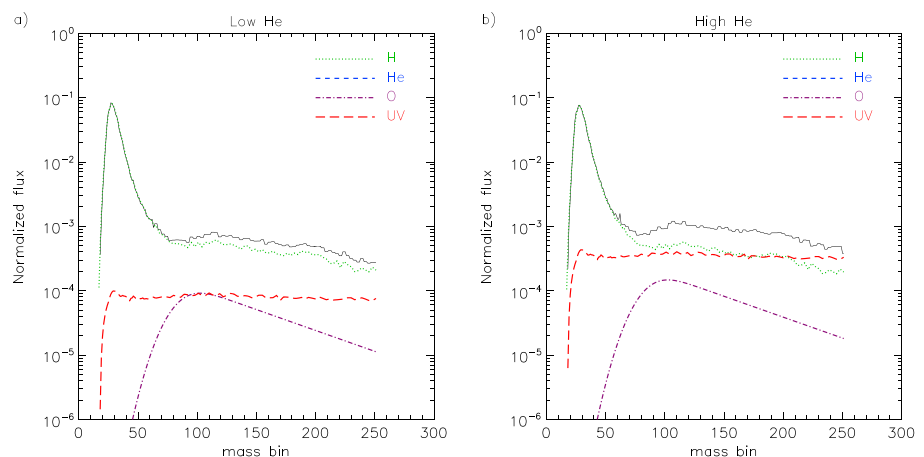


Figure 5. Complete energy range (low energy + high energy) of the measured mass spectra (a) for the low helium group and (b) for the high helium group. Shown are the average measured mass spectra (solid black) and the best fits for H (green dotted), He (blue dashed; nonexistent), O (purple dash-dotted), and UV (red long dashed).

Table 4. Hydrogen-to-Oxygen Flux Ratio for the Two Solar Wind Types During Which the Measurements Were Conducted^a

He Fraction	$\Phi_{\text{H}}^{\text{bs}} / \Phi_{\text{O}}^{\text{sp}} \Big _{\text{meas}}$	$\Phi_{\text{H}}^{\text{bs}} / \Phi_{\text{O}}^{\text{sp}} \Big _{\text{theo}} P = 50\%$	$\Phi_{\text{H}}^{\text{bs}} / \Phi_{\text{O}}^{\text{sp}} \Big _{\text{theo}} P = 25\%$
low	5.4	5.3	2.7
high	2.5	4.6	2.3

^aThe first column shows the ratio obtained from our measurements, and the second and third column show the ratio computed according to sputter and backscatter theory for lunar surface regolith porosity values of $P = 0.5$ and $P = 0.25$, respectively.

$\frac{\epsilon_{\text{O}}^{\text{det}}}{\epsilon_{\text{H}}^{\text{det}}}$ was determined to be equal to $\sim 4.67 \cdot 10^{-2}$ and $\sim 3.77 \cdot 10^{-2}$ for the two solar wind types. Since the sputter and the backscatter energy distribution functions are both normalized to one, the theoretical backscattered hydrogen to sputtered oxygen flux is given by

$$\frac{\Phi_{\text{H}}^{\text{bs}}}{\Phi_{\text{O}}^{\text{sp}} \Big|_{\text{theo}}} = \frac{R_{\text{H}}}{Y_{\text{O}}^{\text{sp}}}. \quad (5)$$

Table 4 lists the measured and the theoretical flux ratios for the low and the high helium groups, computed according to these two equations. The main errors for the measured ratios arise due to uncertainties in the detection efficiencies and from the fit procedure. We estimate to have a relative error of at least 30%.

5. Discussion

To resolve the mass spectra recorded by CENA, we first determined the spectral shapes of hydrogen, helium, oxygen, and UV. Whereas the reference spectra for helium and oxygen were determined from calibration data, the reference spectra for hydrogen and UV were newly determined from in-flight data. The hydrogen reference spectrum was computed from measurements that were conducted when the solar wind consisted of almost pure hydrogen and agrees well with previously determined hydrogen calibration data spectra. The UV spectral shape is flat, except for a small peak at the same position where hydrogen shows up. This peak can be attributed to the fact that the UV spectral shape was determined from actual in-flight data, which contains besides the UV contaminated signal also a small hydrogen signal. The otherwise flatness of the curve is well understood and has already been observed previously for similar instruments [Galli *et al.*, 2006]. Fitting of the in-flight mass spectra with the different reference spectra resulted in the detection of a robust oxygen signal. Whereas the measured oxygen content could be easily compared with sputter theory, a further division of the oxygen signal into individual energy steps is statistically not feasible.

In a first analysis, we compared the oxygen content in CENA's mass spectra, which were divided into two groups: One group contains mass spectra that were recorded when the solar wind consisted of almost pure hydrogen, and the other group contains mass spectra that were recorded when the helium fraction in the solar wind was very high. Since helium is a very effective sputter agent, a clear difference in the sputter yield for these two solar wind types is expected. In our analysis, though, this difference has been diminished to a large extent by the fact that the solar wind flux was more than 50% higher during the low helium group than during the high helium group. Overall, the high helium content solar wind type is supposed to sputter 20% more oxygen from the lunar surface than the low helium content solar wind type. The ratio computed from our measurements is, after having subtracted the respective backgrounds, ~ 1.6 . As one can see from Figure 6, the curve belonging to the solar wind of type 1 drops off much sooner than the curve belonging to the solar wind of type 2. It is therefore well possible that we slightly underestimated the oxygen content in the low helium group. Considering the limited statistics and that the oxygen signal is very small compared to the hydrogen signal, our computed value is in very good agreement with the theoretical value.

In a second analysis, we compared the backscattered hydrogen flux to the sputtered oxygen flux. According to sputter and backscatter theory, this ratio should be equal to ~ 5.3 and ~ 4.6 for the solar wind conditions under which our measurements were conducted. The ratios obtained from our measurements are 5.4 and 2.5. As theory predicts, the low helium group has a higher hydrogen-to-oxygen ratio than the high helium group. Both values agree well with the predictions, especially when considering all approximations necessary to compute the theoretical values and the uncertainties contained in the measurements. In section 4

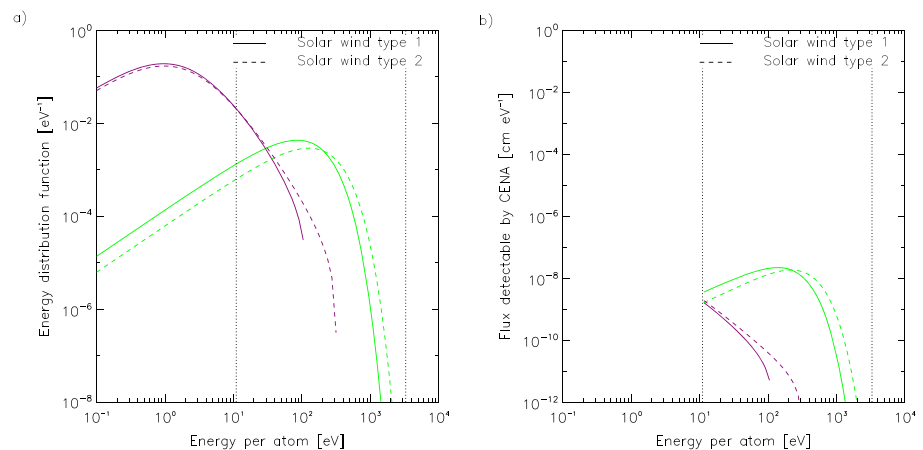


Figure 6. (a) Energy distribution function for sputtered oxygen (purple) and energy distribution function for backscattered hydrogen (green). (b) The product between the oxygen sputter yield, the sputter energy distribution function, and CENA's geometric factor for oxygen (purple) and the product between the hydrogen backscatter ratio, the backscatter energy distribution function, and CENA's geometric factor for hydrogen (green). All curves are given for two solar wind types. Type 1 has a He content of 0.35% and a proton velocity 321 km s⁻¹ (solid line), and type 2 has a He content of 4.57% and a proton velocity of 472 km s⁻¹ (dashed line). The dotted vertical lines show the energy range within which CENA detects particles.

we mentioned that the porosity linearly scales the surface sputter yield. For more information on porosity and its expected influence on the sputter yield, we advise the reader to turn to *Cassidy and Johnson* [2005]. *Wurz et al.* [2007] mention that porosity values of 20% to 80% are plausible. If the porosity were reduced from 50% to 25%, the theoretical values would scale accordingly, i.e., become ~ 2.7 and ~ 2.3 . As one can see from Table 4, our values lie somewhere between these theoretical values.

A robust helium signal was found to be present in the high-energy part of the mass spectra belonging to the high helium group. Since the backscattered helium content linearly scales with the solar wind helium content, it is not expected to be present in the low helium group mass spectra. The lack of a helium signal in the low helium group therefore agrees with backscatter theory. Solar wind helium has 4 times the energy of solar wind hydrogen. If the energy loss during interaction with the surface is similar for these two species, then backscattered helium should show up at 4 times the energy of backscattered hydrogen. *Futaana et al.* [2012] determined from CENA data a characteristic backscattered hydrogen energy of ~ 100 eV. Helium should therefore show up at energies ~ 400 eV. The presence of helium only at energies > 320 eV and the lack thereof at energies < 320 eV is therefore in agreement with backscatter theory.

It is difficult to make a quantitative analysis of the helium content similar to the one we presented for oxygen, since we do not have any information on CENA's detection efficiency for helium. A simple estimation can help verify the credibility of this signal, though. Assuming that helium is backscattered from the lunar surface to the same extent as hydrogen, and that CENA's detection efficiency is the same for these two species, a helium signal smaller than 5% of the hydrogen signal is expected. In reality, CENA's helium detection efficiency is much smaller than CENA's hydrogen detection efficiency because of the much higher ionization potential of helium. Moreover, the backscattered helium ratio is also expected to be smaller than the hydrogen ratio because helium impacts the lunar surface with 4 times the energy of hydrogen. Reflection ratios in the range $(0.5-5) \cdot 10^{-3}$ are therefore plausible. The measured helium to hydrogen ratio is, with being $0.37 \cdot 10^{-3}$, compatible with these estimated values.

Our helium to hydrogen ratio yields a helium backscatter ratio of $1.4 \cdot 10^{-3}$, assuming a hydrogen backscatter ratio of 0.16. As noted above, this helium backscatter ratio is a lower limit, and we estimate that the actual value is about 10 times higher. *Hoffman et al.* [1973] presented Apollo 17 observations that inferred atmospheric helium number densities of $2 \cdot 10^9$ m⁻³ for the lunar dayside. Based on our considerations, the backscattered helium density is estimated to be 10^5-10^6 times smaller than the thermal helium density. This makes it extremely difficult to distinguish backscattered helium from thermal helium in spectroscopic data. Because of the correlation of our helium signal with the solar wind helium content, the energy range at which the signal shows up, and the fact that thermal exospheric helium is of too low energy to be detected by CENA, we conclude that we observed for the first time backscattered helium in the lunar exosphere.

Wurz *et al.* [2007] computed for solar wind fluxes in the range $(2.0\text{--}2.7) \cdot 10^{12} \text{ m}^{-2} \text{ s}^{-1}$ and a helium content of 5%, oxygen surface densities of $\sim (6\text{--}10) \cdot 10^6 \text{ m}^{-3}$ for different lunar soil types. Cook *et al.* [2013] recently presented an observational upper bound for oxygen of $\sim 5.4 \cdot 10^6 \text{ m}^{-3}$ based on measurements conducted by the Lyman Alpha Mapping Project onboard NASA's Lunar Reconnaissance Orbiter. With average solar wind helium contents, particle velocities, particle fluxes, and sputtered yields as presented in the last rows of Tables 1 and 2, oxygen subsolar surface densities of $N_0 = (1.1 \pm 0.3) \cdot 10^7 \text{ m}^{-3}$ and $(1.4 \pm 0.4) \cdot 10^7 \text{ m}^{-3}$, respectively, can be inferred from our results. Note that these densities are valid for the subsolar point, since we computed them assuming a hydrogen backscatter ratio of 16%, which is valid for the subsolar point [Vorburger *et al.*, 2013]. As the hydrogen backscattered ratio varies with the cosine of the solar zenith angle [Wieser *et al.*, 2009], the oxygen surface density should also vary with the cosine of the solar zenith angle. It is possible that our results slightly overestimate the surface densities, but considering that the sputter yield directly scales with the solar wind particle flux and angle of arrival, our values agree very well with both model predictions and the observationally determined upper limits. Applying N_c/N_0 ratios as determined from the model presented in Wurz and Lammer [2003], these surface densities result in column densities of $N_c = (1.5 \pm 0.5) \cdot 10^{13} \text{ m}^{-2}$ and $(1.6 \pm 0.5) \cdot 10^{13} \text{ m}^{-2}$, respectively.

6. Conclusion

Here we presented the first direct measurements of sputtered lunar oxygen in the Moon's exosphere, detected by the Sub-keV Atom Reflecting Analyzer onboard Chandrayaan-1. Based on our measurements, the backscattered hydrogen flux is 2.5 and 5.4 times higher than the sputtered oxygen flux, depending on the solar wind helium content and particle velocity. With a previously determined hydrogen backscatter ratio of 0.16, this results in total sputter yields of 0.03 and 0.06, respectively.

In addition, CENA conducted the first measurements of solar wind helium ions (alpha particles) that were backscattered from the lunar surface as neutral energetic helium atoms.

With average solar wind particle fluxes of $3.70 \cdot 10^{12} \text{ m}^{-2} \text{ s}^{-1}$ and $2.22 \cdot 10^{12} \text{ m}^{-2} \text{ s}^{-1}$, we inferred oxygen surface densities of $N_0 = (1.1 \pm 0.3) \cdot 10^7 \text{ m}^{-3}$ and $(1.4 \pm 0.4) \cdot 10^7 \text{ m}^{-3}$ and column densities of $N_c = (1.5 \pm 0.5) \cdot 10^{13} \text{ m}^{-2}$ and $(1.6 \pm 0.5) \cdot 10^{13} \text{ m}^{-2}$ for the two solar wind types under which the measurements were conducted. These values agree well with model predictions and are consistent with a recently presented new observational upper bound for lunar oxygen surface density.

These first observations of sputtered lunar oxygen and backscattered solar wind helium atoms are a critical contribution for understanding the lunar exosphere origin and microphysics of plasma-surface interactions. Knowledge of these processes will be especially valuable for interpretation of the measurements of the Galilean Moons' exospheres, which will be recorded during the Jupiter Icy Moon Explorer mission as of 2030.

Appendix A: Determination of CENA's Detection Efficiency Ratio of Sputtered Oxygen to Backscattered Hydrogen

According to the definitions of CENA's geometric factors, the ratio between CENA's detection efficiencies for two different species is equal to the ratio between CENA's geometric factors for these species

$$\frac{\epsilon_O^{\text{det}}}{\epsilon_H^{\text{det}}} = \frac{GF_O(E)}{GF_H(E)}, \quad (\text{A1})$$

where ϵ_O^{det} and ϵ_H^{det} are CENA's detection efficiencies for oxygen and hydrogen, respectively, and where $GF_O(E)$ and $GF_H(E)$ are CENA's geometric factors for oxygen and hydrogen, respectively.

CENA's geometric factor for hydrogen has already been determined for certain energies (see below) [Wieser, 2012]. The difference in the geometric factor for oxygen and hydrogen mainly arises at the MgO conversion surfaces, where oxygen and hydrogen atoms are ionized with different efficiencies (cf. section 1). The geometric factor for oxygen, $GF_O(E)$, can therefore, to a good approximation, be assumed to be equal to the geometric factor for hydrogen, $GF_H(E)$, multiplied with the ratio of the positive oxygen and hydrogen ionization efficiencies of the MgO conversion surfaces, $\epsilon_O^{\text{ion}}(E)$ and $\epsilon_H^{\text{ion}}(E)$

$$GF_O(E) = GF_H(E) \cdot \frac{\epsilon_O^{\text{ion}}(E)}{\epsilon_H^{\text{ion}}(E)}. \quad (\text{A2})$$

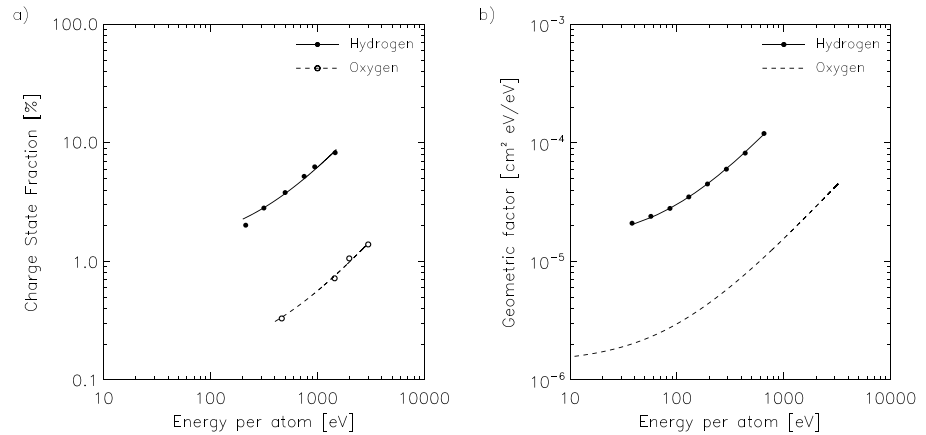


Figure A1. (a) MgO conversion surfaces' charge state fractions [Wieser *et al.*, 2002] and (b) CENA's geometric factors for hydrogen and oxygen. Filled circles and solid lines denote the measurements and the fits for hydrogen, and open circles (where available) and dashed lines denote the measurements and fits for oxygen.

Further, it can be assumed that the ratio of the positive ionization efficiencies for these two species is directly proportional to the ratio between the MgO conversion surfaces' positive charge state fractions for oxygen and hydrogen, $C_O^{\text{ion}}(E)$ and $C_H^{\text{ion}}(E)$

$$\frac{\epsilon_O^{\text{ion}}(E)}{\epsilon_H^{\text{ion}}(E)} = \frac{C_O^{\text{ion}}(E)}{C_H^{\text{ion}}(E)}. \quad (\text{A3})$$

Charge state fractions for MgO surfaces were measured by Wieser *et al.* [2002]. To have a mathematical description of the charge state fractions these measurement points first had to be fitted. In the instrument calibrations no measurements were conducted below ~ 200 eV in the case of hydrogen and ~ 500 eV in the case of oxygen; thus, we do not know what shape the fit function should have at low energies. Theory and measurements [e.g., Los and Geerlings, 1990] suggest that an exponential function seems like an appropriate choice, though. Since, especially in the case of primary neutral oxygen, only few measurements for positive ionization were available, we included measurement points for primary O^+ and O_2^+ as well as H^+ and H_2^+ . Inclusion of positively charged primary particles is supported by the fact that Wieser *et al.* [2002] obtained within the measurement uncertainties the same charge state fractions for primary neutral and ionized particles. Figure A1a shows the average measured $C_H^{\text{ion}}(E)$ (filled circles) and $C_O^{\text{ion}}(E)$ (open circles) and the computed best fits, which are given by

$$\begin{aligned} C_H^{\text{ion}}(E) &= 146.95 \cdot \exp(E \cdot 3.30 \cdot 10^{-5} \text{eV}^{-1}) - 145.65 \\ C_O^{\text{ion}}(E) &= 25.81 \cdot \exp(E \cdot 1.62 \cdot 10^{-5} \text{eV}^{-1}) - 25.66. \end{aligned} \quad (\text{A4})$$

CENA's geometric factor for hydrogen integrated over the solid angle, $GF_H(E)$, was determined from CENA calibration data for eight different energies [Wieser, 2012]. These eight measurement points are presented in Figure A1b (filled circles), together with their best fit (solid line), which is given by the following equation:

$$GF_H(E) = 1.44 \cdot 10^{-5} \text{cm}^2 + E \cdot 1.60 \cdot 10^{-7} \frac{\text{cm}^2}{\text{eV}}. \quad (\text{A5})$$

Having derived a mathematical description of $GF_H(E)$, CENA's geometric factor for oxygen, $GF_O(E)$, can be computed from equations (7) to (10). The thus obtained function is shown by the dashed line in Figure A1b.

As mentioned in the main text, since we are interested in the complete hydrogen-to-oxygen flux ratio, and not just in the flux ratio in CENA's energy range, we have to take into account that CENA only covers a certain fraction of the backscatter and sputter energy distributions ($f_H^{\text{bs}}(E)$ and $f_O^{\text{sp}}(E)$). We thus introduce a new ratio, $\hat{\epsilon}_O^{\text{det}} / \hat{\epsilon}_H^{\text{det}}$, which is given by

$$\frac{\hat{\epsilon}_O^{\text{det}}}{\hat{\epsilon}_H^{\text{det}}} = \frac{\int_{11 \text{eV}}^{3.3 \text{keV}} \epsilon_O^{\text{det}} \cdot f_O^{\text{sp}}(E) dE / \int_{11 \text{eV}}^{3.3 \text{keV}} f_O^{\text{sp}}(E) dE}{\int_{11 \text{eV}}^{3.3 \text{keV}} \epsilon_H^{\text{det}} \cdot f_H^{\text{bs}}(E) dE / \int_{11 \text{eV}}^{3.3 \text{keV}} f_H^{\text{bs}}(E) dE}, \quad (\text{A6})$$

that not only includes CENA's detection efficiencies but also corrects for the limited energy range within which observations can be conducted. This ratio was computed for the two solar wind types to be equal to $\sim 4.67 \cdot 10^{-2}$ and $\sim 3.77 \cdot 10^{-2}$.

Acknowledgments

A. Vorburger and P. Wurz gratefully acknowledge the financial support by the Swiss National Science Foundation. Solar wind parameters from the WIND spacecraft were used as a reference for this study. The authors thank K.W. Ogilvie (NASA/GSFC) and A.J. Lazarus (MIT) for providing WIND data. The efforts at Space Physics Laboratory, Vikram Sarabhai Space Centre, are supported by the Indian Space Research Organisation (ISRO).

Philippa Browning thanks the reviewers for their assistance in evaluating this paper.

References

- Barabash, S., et al. (2009), Investigation of the solar wind-Moon interaction onboard Chandrayaan-1 mission with the SARA experiment, *Curr. Sci.*, *96*(4), 526–532.
- Bhardwaj, A., S. Barabash, Y. Futaana, Y. Kazama, K. Asamura, R. Sridharan, M. Holmström, P. Wurz, and R. Lundin (2005), Low energy neutral atom imaging on the Moon with the SARA instrument aboard Chandrayaan-1 mission, *J. Earth Syst. Sci.*, *114*(6), 749–760, doi:10.1007/BF02715960.
- Cassidy, T., and R. Johnson (2005), Monte Carlo model of sputtering and other ejection processes within a regolith, *Icarus*, *176*, 499–507, doi:10.1016/j.icarus.2005.02.013.
- Cook, J., S. Stern, P. Feldman, G. Gladstone, K. Retherford, and C. Tsang (2013), New upper limits on numerous atmospheric species in the native lunar atmosphere, *Icarus*, *225*, 681–687, doi:10.1016/j.icarus.2013.04.010.
- Flynn, B., and S. Stern (1996), A spectroscopic survey of metallic species abundances in the lunar atmosphere, *Icarus*, *124*, 530–535.
- Futaana, Y., S. Barabash, M. Holmström, and A. Bhardwaj (2006), Low energy neutral atoms imaging of the Moon, *Planet. Space Sci.*, *54*, 132–143, doi:10.1016/j.pss.2005.10.010.
- Futaana, Y., S. Barabash, M. Wieser, M. Holmström, A. Bhardwaj, M. B. Dhanya, R. Sridharan, P. Wurz, A. Schaufelberger, and K. Asamura (2010), Protons in the near-lunar wake observed by the Sub-keV Atom Reflection Analyzer on board Chandrayaan-1, *J. Geophys. Res.*, *115*, A10248, doi:10.1029/2010JA015264.
- Futaana, Y., S. Barabash, M. Wieser, M. Holmström, C. Lue, P. Wurz, A. Schaufelberger, A. Bhardwaj, M. B. Dhanya, and K. Asamura (2012), Empirical energy spectra of neutralized solar wind proton from the lunar regolith, *Geophys. Res. Lett.*, *117*, E05005, doi:10.1029/2011JE004019.
- Galli, A., P. Wurz, H. Lammer, H. Lichtenegger, R. Lundin, S. Barabash, A. Grigoriev, M. Holmström, and H. Gunell (2006), The hydrogen exospheric density profile measured with ASPERA-3/NPD, *Space Sci. Rev.*, *126*, 447–467.
- Gorenstein, P., and P. Bjorkholm (1973), Detection of radon emanation from the crater Aristarchus by the Apollo 15 alpha particle spectrometer, *Science*, *179*(4075), 792–794.
- Goswami, J., and M. Annadurai (2009), Chandrayaan-1: India's first planetary science mission to the Moon, *Curr. Sci.*, *96*(4), 486–491.
- Hoffman, J., and R. Hodges (1975), Molecular gas species in the lunar atmosphere, *The Moon*, *14*, 159–167, doi:10.1007/BF00562981.
- Hoffman, J., R. Hodges, F. Johnson, and D. Evans (1973), Lunar atmospheric composition results from Apollo 17, *Proc. Lunar Sci. Conf.*, *4*, 2865–2875.
- Kazama, Y., S. Barabash, M. Wieser, K. Asamura, and P. Wurz (2007), Development of an LENA instrument for planetary missions by numerical simulations, *Planet. Space Sci.*, *55*, 1518–1529, doi:10.1016/j.pss.2006.11.027.
- Lawson, S., W. Feldman, D. Lawrence, K. Moore, R. Elphic, R. Belian, and S. Maurice (2005), Recent outgassing from the lunar surface: The Lunar Prospector Alpha Particle Spectrometer, *J. Geophys. Res.*, *110*, E09009, doi:10.1029/2005JE002433.
- Los, J., and J. Geerlings (1990), Charge exchange in atom-surface collisions, *Phys. Rep.*, *130*(3), 133–190.
- Lue, C., Y. Futaana, S. Barabash, M. Wieser, M. Holmström, A. Bhardwaj, M. B. Dhanya, and P. Wurz (2011), Strong influence of lunar crustal fields on the solar wind flow, *Geophys. Res. Lett.*, *38*, L03202, doi:10.1029/2010GL046215.
- McCann, D., S. Barabash, H. Nilsson, and A. Bhardwaj (2007), Miniature ion mass analyser, *Planet. Space Sci.*, *55*(9), 1190–1196, doi:10.1016/j.pss.2006.11.020.
- McComas, D., et al. (2009), Lunar backscatter and neutralization of the solar wind: First observations of neutral atoms from the Moon, *Geophys. Res. Lett.*, *36*, L12104, doi:10.1029/2009GL038794.
- Potter, A., and E. Morgan (1988), Discovery of sodium and potassium vapor in the atmosphere of the Moon, *Science*, *241*(4866), 675–680, doi:10.1126/science.241.4866.675.
- Saito, Y., et al. (2008), Solar wind proton reflection at the lunar surface: Low energy ion measurements by MAP-PACE onboard SELENE (KAGUYA), *Geophys. Res. Lett.*, *35*, L24205, doi:10.1029/2008GL036077.
- Sarantos, M., R. Killen, D. Glenar, M. Benna, and T. Stubbs (2012), Metallic species, oxygen and silicon in the lunar exosphere: Upper limits and prospects for LADEE measurements, *J. Geophys. Res.*, *117*, A03103, doi:10.1029/2011JA017044.
- Stern, S. A. (1999), The lunar atmosphere: History, status, current problems, and context, *Rev. Geophys.*, *37*(4), 453–491, doi:10.1029/1999RG900005.
- Stern, S. A., J. Cook, J.-Y. Chaufray, P. Feldman, G. Gladstone, and K. Retherford (2013), Lunar atmospheric H₂ detections by the LAMP UV spectrophotometer on the Lunar Reconnaissance Orbiter, *Icarus*, *226*, 1210–1213, doi:10.1016/j.icarus.2013.07.011.
- Tyler, A., W. Kozłowski, and D. Hunten (1988), Observations of sodium in the tenuous lunar atmosphere, *Geophys. Res. Lett.*, *10*(15), 1141–1144, doi:10.1029/GL015i010p01141.
- Vorburger, A., P. Wurz, S. Barabash, M. Wieser, Y. Futaana, C. Lue, M. Holmström, A. Bhardwaj, M. B. Dhanya, and K. Asamura (2013), Energetic neutral atom imaging of the lunar surface, *J. Geophys. Res. Space Physics*, *118*, 3937–3945, doi:10.1002/jgra.50337.
- Wieser, M. (2012), *CENA FM Calibration Report: Issue 1 Revision 2*, Swedish Institute of Space Physics, IRF, Kiruna, Sweden.
- Wieser, M., P. Wurz, K. Brünnig, and W. Heiland (2002), Scattering of atoms and molecules off a magnesium oxide surface, *Nuc. Instr. Meth. Phys. Res. B*, *192*, 370–380.
- Wieser, M., S. Barabash, Y. Futaana, M. Holmström, A. Bhardwaj, R. Sridharan, M. Dhanya, P. Wurz, A. Schaufelberger, and K. Asamura (2009), Extremely high reflection of solar wind protons as neutral hydrogen atoms from regolith in space, *Planet. Space Sci.*, *57*, 2132–2134, doi:10.1016/j.pss.2009.09.012.
- Wurz, P. (2001), Heavy ions in the solar wind: Results from SOHO/CELIAS/MTOF, Universität Bern, Bern, Switzerland.
- Wurz, P., and H. Lammer (2003), Monte-Carlo simulation of Mercury's exosphere, *Icarus*, *164*, 1–13, doi:10.1016/S0019-1035(03)00123-4.
- Wurz, P., U. Rohner, J. A. Whitby, C. Kolb, H. Lammer, P. Dobnikar, and J. A. Martín-Fernández (2007), The lunar exosphere: The sputtering contribution, *Icarus*, *191*, 486–496, doi:10.1016/j.icarus.2007.04.034.